Structure
Article

Insights into the Structure and Domain Flexibility of Full-Length Pro-Matrix Metalloproteinase-9/Gelatinase B

Gabriel Rosenblum,[1,6] Philippe E. Van den Steen,[2,6] Sidney R. Cohen,[3,6] J. Günter Grossmann,[4] Jessica Frenkel,[1] Rotem Sertchook,[1] Nelle Slack,[5] Richard W. Strange,[4] Ghislain Opdenakker,[2] and Irit Sagi[1,*]
[1]Department of Structural Biology, The Weizmann Institute of Science, Rehovot 76100, Israel
[2]Laboratory of Immunobiology, Rega Institute for Medical Research, University of Leuven, 3000 Leuven, Belgium
[3]Chemical Research Support, The Weizmann Institute of Science, Rehovot 76100, Israel
[4]Molecular Biophysics Group, Science and Technology Facilities Council Daresbury Laboratory, Warrington WA4 4AD, United Kingdom
[5]VEECO Metrology Division, Santa Barbara, CA 93117, USA
[6]These authors contributed equally to this work.
*Correspondence: irit.sagi@weizmann.ac.il
DOI 10.1016/j.str.2007.07.019

SUMMARY

The multidomain zinc endopeptidase matrix metalloproteinase-9 (MMP-9) is a recognized therapeutic target in autoimmune diseases, vascular pathologies, and cancer. Despite its importance, structural characterization of full-length pro-MMP-9 is incomplete. Here, we report the structural model of full-length pro-MMP-9 and, in particular, the molecular character of its unique proline-rich and heavily O-glycosylated (OG) domain. Using a powerful combination of small-angle X-ray scattering and single-molecule imaging, we demonstrate that pro-MMP-9 possesses an elongated structure with two terminal globular domains connected by an unstructured OG domain. Image analysis highlights the flexibility of the OG domain, implicating its role in the varied enzyme conformations and in facilitating independent movements of the terminal domains. This may endorse recognition, binding, and processing of substrates, ligands, as well as receptors and marks this domain as an additional target for the design of selective regulators.

INTRODUCTION

The physiological and pathological roles of matrix metalloproteinases (MMPs) are versatile. Members of the MMP family have been implicated in numerous aspects of the migration of inflammatory and cancer cells through connective tissues, not only by catabolizing extracellular matrix (ECM) components, but also by processing various soluble mediators, promoting many disease states (Stetler-Stevenson et al., 1993; Werb and Chin, 1998; Wolf et al., 2003). Although all MMPs share similar catalytic sites (Maskos, 2005), marked differences are observed in their substrate specificity, due, at least in part, to the presence of additional substrate-binding sites in noncatalytic protein domains. As a consequence, different MMPs have different biological functions. MMP-9, also known as gelatinase B, is a prototypical target in inflammatory diseases, because of its tissue-damaging roles (Agrawal et al., 2006; Liu et al., 1998; Opdenakker et al., 2003; Van den Steen et al., 2004) and inflammation-promoting processing of soluble proteins, including protease inhibitors (Liu et al., 2000), chemokines (Van den Steen et al., 2000), and cytokines (Heissig et al., 2002; Nelissen et al., 2003; Yu and Stamenkovic, 2000).

In contrast, MMP-2, or gelatinase A, mainly has anti-inflammatory and homeostatic functions, and it presumably acts by inactivating inflammatory chemokines (McQuibban et al., 2000) and by regulating connective tissue turn-over (Monaco et al., 2006). This functional dichotomy between both enzymes has clearly been demonstrated in several knockout studies (Garg et al., 2006; Itoh et al., 2002). It also implies that selective inhibitors, discriminating between these highly similar enzymes, are crucial for efficient anti-inflammatory therapy without side effects (Hu et al., 2007). From this perspective, other noncatalytic parts of the enzyme, differentiating MMP-2 and MMP-9, may be targeted to generate selective inhibitors.

Interestingly, the main structural difference between MMP-9 and MMP-2 is the presence of an extensively O-glycosylated (OG) domain in MMP-9 (Opdenakker et al., 2001; Van den Steen et al., 2006). Other domains in MMP-9 are also found in MMP-2 and include a propeptide domain responsible for maintaining latency; a catalytic domain in which three fibronectin repeats are inserted; and a C-terminal domain, also known as the hemopexin domain, that constitutes an exosite for binding of the endogenous MMP-9 inhibitor, tissue inhibitor of metalloproteinase 1 (TIMP-1) (Piccard et al., 2007; Wilhelm et al., 1989). Despite its great importance in many disease states and in contrast to MMP-2 (Morgunova et al., 1999), the available structural information about

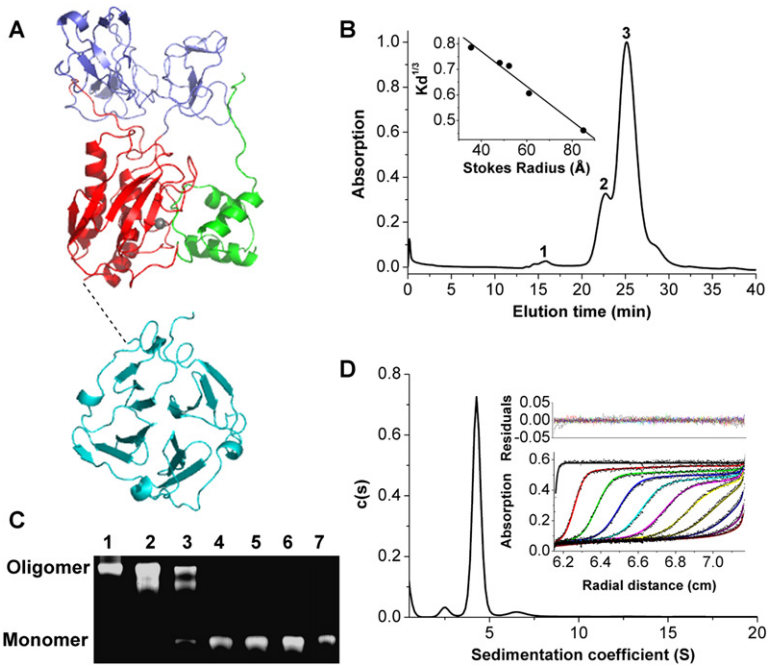

Figure 1. Characterization of Pro-MMP-9

(A) Crystal structures of the terminal domains. The N-terminal domain of pro-MMP-9 (PDB code: 1L6J) is comprised of the propeptide (green), three fibronectin type-II repeats (blue), and a catalytic domain (red) with the zinc-containing active site (gray sphere). The OG domain (dashed line) contains a 64 residue fragment of unknown structure, and it connects the N-terminal domain to the C-terminal hemopexin domain (PDB code: 1ITV), which consists of four propeller blades (cyan).

(B) Size-exclusion chromatography shows the elution profile of oligomeric species (peak 1, 15.8 min; peak 2, 22.7 min) and monomeric (peak 3, 25.1 min) forms of pro-MMP-9. Inset: Porath plot (Siegel and Monty, 1966) of protein standards with known Stokes radii were used to calibrate the superdex 200 column (from right to left: thyroglobulin, 85 Å; ferritin, 61 Å; catalase, 52.2 Å; aldolase, 48.1 Å; albumin, 35.5 Å). The cubic root of K_d is plotted against the Stokes radius of each protein, and the linear least-square fit is shown.

(C) Glycerol sedimentation was applied in order to separate monomers from higher oligomeric structures in preperative amounts. Aliquots from each fraction were assayed in a gelatin zymogram. High oligomeric structures are present in fractions 1–3. Fraction 3 contained a mixture of all oligomeric forms. Fractions 4–7 mostly contained the monomeric form.

(D) Analytical ultracentrifugation sedimentation velocity analysis was used to calculate the distribution of the sedimentation coefficient. Inset: modeling the sedimentation profiles (lines) from the experimental data (dots) as a function of time and distance from the axis of rotation. A residuals plot is shown in the upper panel. For clarity, only every tenth profile used in the analysis is shown.

MMP-9 is limited to its two terminal domains, rather than the full-length enzyme. The X-ray structure of the N-terminal part (Elkins et al., 2002), containing the procatalytic domain, shows that it possesses a matrixin fold (Stocker and Bode, 1995). The C-terminal hemopexin domain consists of a four-bladed β propeller structure with pseudo four-fold symmetry (Cha et al., 2002). Figure 1A presents the crystal structures of the procatalytic and the hemopexin domains of pro-MMP-9. The domains are connected by a dotted line representing the 64 amino acid linker (containing 22 proline residues, 6 glycine residues, and ~12–14 O-linked glycans [Van den Steen et al., 2001]). Importantly, the OG domain of pro-MMP-9 is 2–3 times longer than analogous regions of collagenases, stromelysins, and gelatinase A, of the MMP family, for which typical linker lengths span a range of only 21–27 amino acid residues.

Crystallization of the OG domain in pro-MMP-9 separately or together with other protein domains has been proven difficult. The lack of a large side chain in the case of glycine and the presence of a built-in bend in the case of proline interfere with the formation of secondary structure and often result in loops or unstructured regions. In addition, the presence of clustered serines and threonines as attachment points for O-glycans might yield steric effects that could hinder crystallographic packing. This domain has also been termed the collagen V-like domain, due to its sequence similarity to collagen V (Wilhelm et al., 1989), and has recently been renamed the OG domain (Van den Steen et al., 2006). The OG domain is active in the orientation of the hemopexin domains to enable exosite interactions. However, nothing is known of the influence of the OG domain on the overall three-dimensional structure of MMP-9 and its biophysical nature.

Here, we report on a powerful structural analysis combining small-angle X-ray scattering (SAXS) with single-molecule atomic force microscopy (AFM) imaging to characterize a full-length structural model of pro-MMP-9 and the molecular character of its OG linker domain. SAXS followed by image and structural reconstruction analyses provided the molecular shape of full-length pro-MMP-9, which represents the sum of all possible conformations in solution. This structural model, which is supported by high-resolution AFM imaging and biophysical measurements, shows an elongated protein with the OG domain acting as a flexible 30 Å long linker between the two terminal domains. The degree of flexibility of the OG domain is statistically evaluated from the various protein conformations detected by single-molecule imaging. This provides insights into the role of protein domain flexibility in the regulation of recognition, binding, and processing of substrates, ligands, and receptors required for MMP-9 activities. This suggests that blocking such domain flexibility by antagonists may constitute a way of regulating the pathological activities of this enzyme.

RESULTS AND DISCUSSION

Molecular size and shape determination, structural reconstruction, and analysis of single-molecule images of pro-MMP-9 monomers require monodispersed and homogeneous protein samples. We have therefore combined various methods to express, isolate, and characterize the monomeric form of pro-MMP-9.

Isolation and Characterization of Pro-MMP-9 in Its Monomeric Form

Recombinant pro-MMP-9 was expressed and purified from baculovirus-infected Sf9 cells as previously reported (Van den Steen et al., 2006) (see Experimental Procedures). This enzyme forms mixtures of monomers and other higher oligomeric species (Wilhelm et al., 1989). Dimers of MMP-9 are detected under physiological conditions (Olson et al., 2000). These dimers are resistant to dissociation by SDS, are sensitive to chemical reduction, and require the presence of the OG domain to be formed. The monomeric form of MMP-9 is stable, and no dynamic equilibrium between the monomer and higher oligomeric states are observed (Van den Steen et al., 2006). In this work, we have focused on the structural characterization of the monomeric form of pro-MMP-9.

Figure 1B shows the relative molecular ratio of pro-MMP-9 monomer to its oligomeric species, as determined by analytical size-exclusion chromatography (SEC). The main peak (No. 3) in the chromatogram comprises the pro-MMP-9 monomer with a Stokes radius of 45.4 Å (see inset). The Stokes radius was determined based on the corresponding retention time by using conventional procedures (see the Supplemental Data available with this article online).

Isolation of pro-MMP-9 monomers from higher oligomeric species in preparative amounts was achieved by glycerol-gradient sedimentation (Olson et al., 2000). Figure 1C shows zymography analysis of the various fractions (see the Supplemental Data). The isolated monomer fraction was subjected to analytical ultracentrifugation (AUC) for additional estimation of its Stokes radius (Figure 1D). In this sedimentation velocity experiment, a uniform pro-MMP-9 solution is subjected to a gravimetric field. This produces a depletion of solute near the meniscus and the formation of a sharp boundary between the depleted region and the sedimenting solute (which is of uniform concentration) (Figure 1D, inset). The rate of movement of this boundary can be measured and leads to the determination of the sedimentation coefficients, which depends directly on the mass of the particles and inversely on the frictional ratio, which is, in turn, a measure of effective size and shape (see the Supplemental Data).

The pro-MMP-9 monomer was found to sediment as a single species, with the main peak representing 91% of the total protein in the sample, with a normalized sedimentation coefficient, $s^{\circ}_{20,w}$, of 4.4 S (Figure 1D). This value is compatible with a recent measurement (Van den Steen et al., 2006). A Stokes radius of 44.1 Å was computed with the program SEDNTERP (Laue et al., 1992) by using a calculated partial specific volume of 0.7328 cm^3/g (see the Supplemental Data). Calculation of the molar mass of pro-MMP-9 (see the Supplemental Data and Figure S1) based on the AUC data suggests that this protein is monomeric in solution. AUC-based shape analysis (by using the experimental frictional ratio) indicated that pro-MMP-9 would be hydrodynamically equivalent to a prolate ellipsoid with an estimated axial ratio of 1:6. The molecular radial results obtained by AUC are consistent with the value obtained by SEC (45.4 Å). In addition, theoretical estimation of the radius by applying SEDNTERP and using the pro-MMP-9 molar mass and amino acid and glycan composition yielded a molecular equivalent, spherical radius of 28.7 Å. Deviation of this value from the experimental Stokes radii provides another indication for a nonspherical shape—one that is either elongated or distorted.

Molecular Shape Analysis of Pro-MMP-9 by Small-Angle X-Ray Scattering Reveals an Elongated Three-Domain Structure

The global conformation of the pro-MMP-9 monomer in solution was investigated by using SAXS. This method utilizes the elastic scattering of incident X-ray photons by the target molecule electrons. The electron density distribution, as governed by the arrangement of atoms in the molecule, leads to an interference pattern. The three-dimensional shape of the molecule is then reconstructed from the scattering profile (Svergun and Koch, 2002).

Scattered intensity was observed over a momentum transfer range of $0.008 < q < 0.46$ Å^{-1} ($q = 4\pi\sin\theta/\lambda$) corresponding to a d-spacing range of $14 < r < 785$ Å. The lower value (14 Å) presents the approximate, qualitative nature of the resolution value for the obtained measurements. The scattered intensities are linear in the small-q region (for a scattering profile, see Figure 2A) and are nicely fitted by the Guinier law. The slope was found to be weakly correlated with protein concentration. This means that neither aggregation nor interparticle interference contributes significantly to the signal. In addition, we have used the forward scattered intensity analysis to calculate the molar mass of pro-MMP-9 (Mylonas and Svergun, 2007). For this, we have used a protein standard with a known molecular weight. The details of this analysis are described in the Supplemental Data. In agreement with the AUC result, the SAXS data indicate that pro-MMP-9 retains its monomeric form in solution. The radius of gyration (R_g) resulting from the measurement is 50 ± 2.7 Å. The function p(r) represents the distribution of interatomic distances within the molecule (pair distribution function; Figure 2A, inset). Extraction of R_g from p(r) gives a comparable value, 49.2 Å, indicating accurate preliminary data analysis (prior to the fitting procedure). The maximal interatomic distance (D_{max}) is 160 Å. The shape of p(r) is indicative of an elongated ellipsoid structure (see, for example, Receveur et al., 2002; Violot et al., 2005; von Ossowski et al., 2005).

The three-dimensional reconstruction model of pro-MMP-9 was obtained by using the programs GASBOR

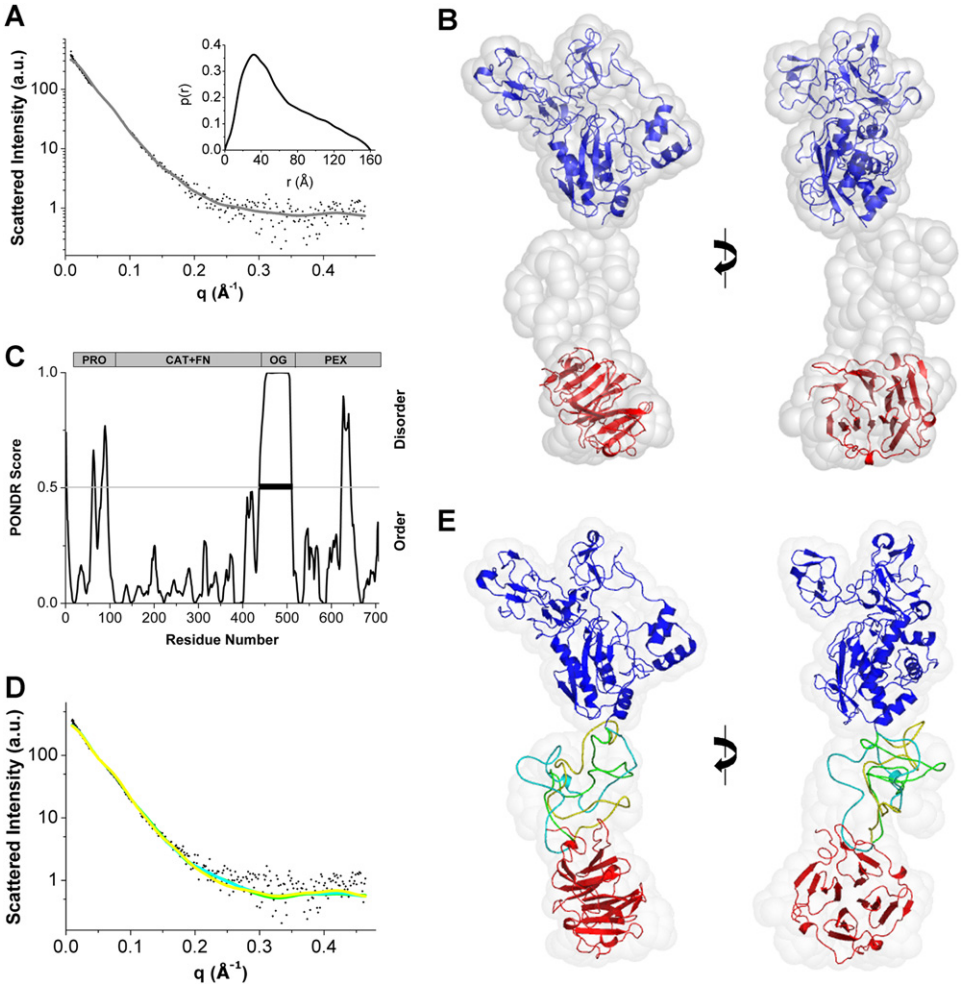

Figure 2. Structural Analysis of Pro-MMP-9

(A) SAXS data of pro-MMP-9 in solution. Experimental X-ray intensity data (black dots) are compared with the most probable model (gray line) by using CHADD. Inset: pair distribution function of the experimental SAXS data.

(B) Pro-MMP-9 models reconstructed by using CHADD. The models obtained from the SAXS data are represented by gray spheres with a radius of 5 Å. Each model was rotated at 0° and 90° along the vertical axis. The docked crystal structures of the N- and C-terminal domains (Cha et al., 2002; Elkins et al., 2002) are represented as blue and red ribbons, respectively.

(C) Prediction of a long-disorder region (thick, black line), by using PONDR (Li et al., 1999), in the sequence of pro-MMP-9 and the corresponding domain organization (top bar: PRO, propeptide; CAT+FN, catalytic domain and three fibronectin type-II repeats; OG, O-glycosylated domain; PEX, hemopexin domain).

(D) Fitting of the calculated scattering curve of the full-length pro-MMP-9 with the reconstructed OG domain to the experimental data. The calculated curves of the best three models are shown as green, cyan, and yellow lines. The experimental data are represented as black dots. The three best models of the OG domain were calculated by using RAPPER (DePristo et al., 2003a, 2003b) within the CHADD model.

(E) Structural reconstruction of the OG domain. The best three models are shown in ribbon representation and are colored green, cyan, and yellow.

(Svergun et al., 2001) and CHADD (Petoukhov et al., 2002). Theoretical scattering curves are simulated from three-dimensional arrangements of spherical centers (or dummy residues) representing protein residues, which combine to form the overall protein shape. The final protein shape is determined by iterative fitting of the simulated theoretical curves to the experimental data. The advantage of CHADD is in the use of a priori knowledge obtained from available crystal structure of isolated domains to introduce constraints in the data analysis procedures. In contrast, models produced by GASBOR are calculated without any a priori knowledge. For clarity, here we report the best model obtained by CHADD (a detailed comparison is described in the Supplemental Data and Figure S2).

Figure 2B shows the three-dimensional reconstructed structural model of pro-MMP-9. The Stokes radius of the reconstructed structure of pro-MMP-9 was calculated by using the program HYDROPRO (Garcia De La Torre et al., 2000). This calculated radius ranges between 44.9 and 47.1 Å, which agrees with the measured values of 45.4 and 44.1 Å obtained by SEC and AUC, respectively. Furthermore, both the SAXS model and the axial ratio

parameter obtained by AUC suggest an elongated shape. Hence, the reconstructed shape restored from the experimental SAXS profile is consistent with the measured hydrodynamic data obtained both by SEC and AUC.

The simulated curve-fitting analysis of this structural model is presented in Figure 2A (gray curve). The location of the alpha carbon backbone of the procatalytic domain was used as a constraint in the structural reconstruction analysis, while the OG and the hemopexin domains were reconstructed by using CHADD. Finally, the crystal structures of the procatalytic (Elkins et al., 2002) domain and the hemopexin domain (Cha et al., 2002) were sequentially docked to the contour density by using the software SUPCOMB (Kozin and Svergun, 2001) (Figure 2B). The remaining density belongs to the OG domain that separates the two terminal domains by ~30 Å. This value was further verified by calculating the theoretical p(r) curves based on the crystal structures of the isolated N-terminal and C-terminal domains by using the software CRYSOL (Svergun et al., 1995). The calculated D_{max} values for these domains are 80 Å and 50 Å, respectively. Subtracting these values from the experimental D_{max} of full-length pro-MMP-9 (160 Å) provides further verification of the reconstructed structure in which the terminal domains are separated by ~30 Å.

Inspecting the volumes occupied by the OG and hemopexin domains reveals that they are of similar volume. However, the calculated molar mass of the OG domain, including the O-glycans, is about half that of the hemopexin domain. Computational sequence analysis of the OG domain by using PONDR (Li et al., 1999) revealed that this region is significantly disordered relative to the other domains (Figure 2C). Thus, despite its observed compact conformation, this proline-rich OG domain possesses a disordered structure of relatively low density. Therefore, the relatively bulky electron density of the OG domain, detected by SAXS, represents the sum of the scattering contribution of the different conformations retained by the OG domain in solution. This suggests that the OG domain is flexible. We have used the structural modeling program RAPPER (DePristo et al., 2003a, 2003b) to model possible linker conformations that will fit the observed scattering profile and density map. Specifically, 8 out of 500 calculated conformers fit the SAXS model of the linker. Theoretical scattering curves were calculated (by using the SAXS program CRYSOL [Svergun et al., 1995]) for the overall pro-MMP-9 model structure. Figures 2D and 2E describe the best linker models that fit both the experimental scattering curve and the SAXS density map of pro-MMP-9. The OG linker appears to exhibit multiple putative, unstructured conformations.

Characterization of Shape and Domain Flexibility of Pro-MMP-9 by Single-Molecule Imaging

To further verify our SAXS analysis, we have designed an experiment to directly visualize the shape of pro-MMP-9, as predicted in Figures 2B and 2E, and to evaluate the molecular properties of its OG domain. Specifically, we conducted single-molecule imaging analysis of wild-type and of an OG-deleted mutant of pro-MMP-9 (pro-MMP-9ΔOG) by using AFM. Reproducible images of single pro-MMP-9 molecules (Figure 3) were obtained by cross-linking the protein samples to an amine-modified silanized layer on a Si(111) surface prior to AFM imaging (see Experimental Procedures and the Supplemental Data for details).

Samples were imaged both under buffer solution and in air (see the Supplemental Data and Figure S4). The best images were obtained in semidry mode with a "spike" tip. Figures 3A–3C show a single-molecule image of wild-type pro-MMP-9 immobilized on the modified Si(111) surface. Consistent with the reported SAXS analysis, the protein image possesses an elongated multidomain structure. The image cross-section (Figure 3C) representing height versus width reveals two separate protein domains presumably connected by the OG linker. In contrast, the pro-MMP-9ΔOG mutant lacking the 64 residue OG domain exhibits a rather spherical shape with unresolved domain separation (Figures 3D–3F).

Single-Molecule Imaging Statistical Analysis Coupled with SAXS Reveals Protein Domain Flexibility Mediated by the OG Domain

A striking feature contrasting the wild-type pro-MMP-9 and the mutant pro-MMP-9ΔOG is that the spread in both width and height values for the wild-type is significantly larger than for the mutant (Figure 4; Table 1; and the Supplemental Data). Such differences could arise from the additional degrees of freedom lent to the wild-type structure by the OG domain, as opposed to the mutant, in which the two lobes are more confined. The heterogeneity of sizes results from two main variables: the different orientations of the protein on the surface and different protein conformations. As the mutant contains no OG domain, it has a reduced conformational heterogeneity, meaning that the spread of values stems mainly from different orientations on the surface.

The effect of the OG domain on protein flexibility is clearly observed in Figure 4E, which reports measurements of lobe-to-lobe distances. The spread of distances ranges from 55 to 85 Å and can be divided into two subpopulations. Remarkably, these results support the existence of multiple enzyme conformations mediated by the flexible molecular nature of the OG domain. Figure 4F presents some possible models of various protein conformations based on the derived lobe-to-lobe distances. The lobe-to-lobe distances were allowed to vary within one standard deviation (9.5 Å). The various OG domain conformations presented in Figure 4F were calculated by using the structural modeling program RAPPER (DePristo et al., 2003a, 2003b).

The protein flexibility of pro-MMP-9, detected by this molecular analysis, provides molecular insights, to our knowledge not previously reported, into the overall structure and molecular character of the enzyme, highlighting the structure-function uniqueness of pro-MMP-9 compared to other members of the MMP family, including gelatinase A/MMP-2 (Morgunova et al., 1999). For instance,

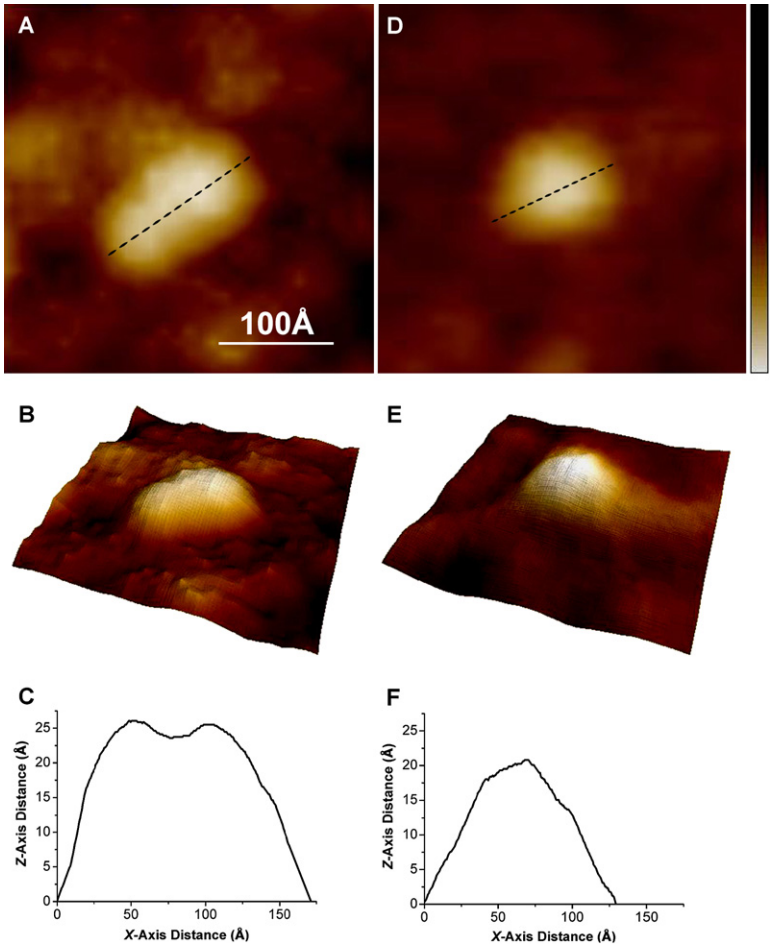

Figure 3. AFM Images of Wild-Type and Mutated Pro-MMP-9

(A–F) Glutaraldehyde served as a covalent linker between the amine on the surface to the protein. All scans employed a spike tip. (A–C) Semidry mode scans of wild-type pro-MMP-9. (D–F) Semidry mode scan of the pro-MMP-9ΔOG mutant. (A) and (D) are two-dimensional (plan-view) representations. (B) and (E) are three-dimensional representations. (C) and (F) are XZ cross-sections along the dashed line shown in (A) and (D). Note the expected reduction in protein length upon deletion of the OG domain. For sample preparation and imaging conditions, see the text. The height scale is indicated by the bar to the right, in which the z axis ranges from 0 to 50 Å (dark to light).

in collagenase-1/MMP-1, the flexibility of a much shorter linker region is further constrained by interactions between the hemopexin domain and the prodomain (Lauer-Fields et al., 2002). Similarly, in MMP-2, the second blade of the hemopexin domain is linked to the fibronectin domain through a hydrogen bond (Morgunova et al., 1999).

The Role of Protein Domain Flexibility in the Enzymatic Function of Pro-MMP-9

MMP-9 is a secreted enzyme, and it is not clear how it is targeted to the right location and how its activity is controlled in the pericellular space (Fridman et al., 2003). Specifically, it is not clear what the roles of the various domains are in mediating effective protein-substrate and protein-protein interactions during catalysis. The full-length structural model of pro-MMP-9 reported here introduces insights into the structure of this enzyme and into its apparent domain flexibility. In particular, the reported results raise the possibility that the terminal domain separation and the observed protein flexibility in MMP-9 are required to mediate its function.

The contribution of the OG domain was postulated in earlier work to be a spacer moiety that allows for independent movement of the terminal domains (Overall, 2002; Rudd et al., 1999; Van den Steen et al., 2006). Interestingly, a bioinformatics "BLAST" search (Altschul et al., 1997; Schaffer et al., 2001) of all of the available databases revealed that the OG domain in pro-MMP-9 is homologous to similar disordered domains in a number of cell surface-associated and ECM-binding proteins (see Table S1). Remarkably, close structural homology was found between the OG linker and the overall domain organization of pro-MMP-9 and the fungi cellulase (Receveur et al., 2002; von Ossowski et al., 2005), for which the role of the linker in cellulase was proposed to mediate protein-cellulose binding and enzyme migration in intact matrices. This suggests that pro-MMP-9 mediates its biological function and enzymatic activities by cell surface association and/or interactions with solid substrates (e.g., ECM).

Recently, Owen et al. (2003) described TIMP-1-resistant MMP-9 activity at the cell surface of neutrophils. One way to achieve tethering of the MMP-9 hemopexin domain to the cell might be through interactions of the MT6-MMP/TIMP-1 complex at the cell surface. Our data suggest that OG domain flexibility allows the N terminus of MMP-9 to access complex substrate networks (e.g., collagen-like molecules) in the pericellular environment. Stabilization of such protein-substrate interactions may be achieved by nonspecific protein-protein interactions

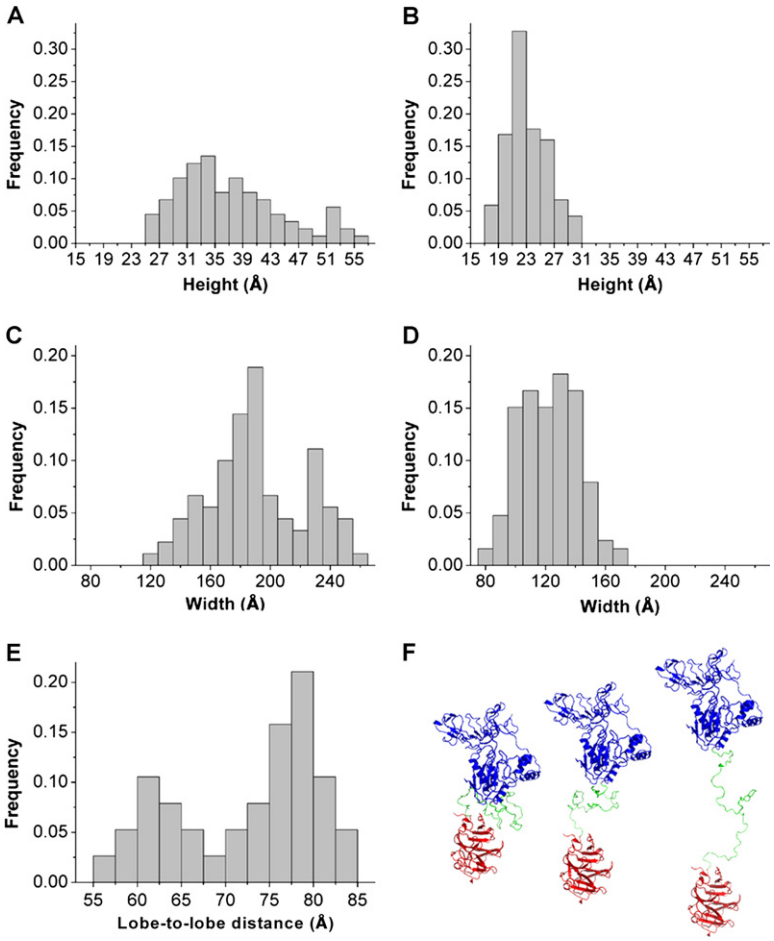

Figure 4. Size Distribution Histograms of the Wild-Type and Pro-MMP-9ΔOG as Measured by AFM

(A–F) The y axis of all histograms is the normalized frequency obtained by dividing the counts by the total population. The left panel represents wild-type pro-MMP-9, and the right panel represents pro-MMP-9ΔOG. (A) and (B) Height distribution. (C) and (D) Width distribution. The width values were corrected as described in the Experimental Procedures. (E) Lobe-to lobe distribution of wild-type pro-MMP-9. The separation between lobes in pro-MMP-9ΔOG could not be resolved. (F) Modeling conformational states of pro-MMP-9. A standard deviation of 9.5 Å, as calculated according to the lobe-to-lobe AFM data, was subtracted or added to the interdomain separation of the averaged structure obtained by SAXS structural reconstruction. The N- and C-terminal domains (Cha et al., 2002; Elkins et al., 2002) are represented by a blue and red cartoon, respectively. The OG domain was reconstructed by using RAPPER (DePristo et al., 2003a, 2003b) and is represented by a green Cα trace.

mediated by the proline-rich sequences (Williamson, 1994) residing in the MMP-9 OG domain. In contrast, the hemopexin domain and the fibronectin domain in pro-MMP-9 were shown to stoichiometrically bind substrates with great affinity (Collier et al., 1992; Roeb et al., 2002).

Importantly, correct interaction with TIMP-1, LRP-1, and megalin requires OG domain involvement to achieve proper orientation of the hemopexin and catalytic domains (Van den Steen et al., 2006). The OG-deleted mutant showed decreased affinity to these molecules, suggesting that the OG domain is essential for regulating the bioavailability of active MMP-9. Although our single-molecule imaging results indicate that the spacing between the terminal domains is not constant, the quasi-globular shape of the OG domain, as obtained by SAXS model reconstruction, ensures minimal separation between the two domains, allowing for binding of regulators to the C-terminal domain without steric hindrance from the N-terminal catalytic domain. Such domain flexibility is not observed for MMP-2. This may explain why MMP-9 can bind directly to LRP-1, while MMP-2 requires the formation of a precursor complex with TIMP-2 (Emonard et al., 2004) or with thrombospondin (Yang et al., 2001) to achieve effective binding to LRP-1.

Table 1. Statistical Analysis of Sizes Obtained by AFM

	Wild-Type	Pro-MMP-9ΔOG
Height	34 (7.5)	22 (2.9)
Width	190 (33)	130 (13)
Lobe-to-lobe	78 (9.5)	N/A

The most probable values are reported, since the presence of two subpopulations may impose a bias on the mean value. Standard deviation is reported in parentheses. The values correspond to the wild type pro-MMP-9 (n = 90) and to the pro-MMP-9ΔOG mutant (n = 120). Lobe-to-lobe distances were measured between the peaks in the XZ cross-section. Values were extracted only if the orientation of the protein on the surface allowed for identification of two distinct domains (n = 83). The separation between lobes in pro-MMP-9ΔOG could not be distinguished. All values are given in angstroms. It is noteworthy that the calculated axial ratio obtained from the most probable height/width values, which represent the ratio between the vertical length and the width of the molecule, is 1:5.6, which is in good agreement with the axial ratio obtained by AUC.

Conclusions

To our knowledge, this work represents the first experimental structural model determination of full-length human

pro-MMP-9 revealed by the combination of structural analyses. A combination of single-molecule imaging and SAXS was utilized to derive a comprehensive molecular model providing structural and dynamic insights into this important enzyme. Remarkably, our results demonstrate the presence of a flexible and unstructured OG domain bridging the catalytic enzyme core and the hemopexin domain. This structure endows pro-MMP-9 with unique domain architecture relative to other family members. Such structural exclusiveness may be utilized for the design of isoform-selective inhibitors for MMP-9. The design of regulators for MMP-9 may be targeted at restricting its domain flexibility, which may block its pathological activity in specific disease states.

EXPERIMENTAL PROCEDURES

Recombinant pro-MMP-9 was expressed by infection of Sf9 insect cells with a baculovirus carrying the cDNA of human pro-MMP-9 (Van den Steen et al., 2006). Liter quantities of cell culture fluids were centrifuged, filtered, and purified to homogeneity by using gelatin-Sepharose chromatography (Masure et al., 1991). The material was extensively dialyzed in 100 mM Tris (pH 7.4), 100 mM NaCl, 10 mM $CaCl_2$ (buffer C) before further processing, and ~20 mg was used in the present study. A mutant lacking the OG domain (MMP-9ΔOG) was prepared in a similar manner (Van den Steen et al., 2006).

Small-Angle X-Ray Scattering

Small-angle X-ray scattering (SAXS) experiments in solution were performed at station 2.1 (Towns-Andrews et al., 1989) of the Synchrotron Radiation Source, Daresbury Laboratory, UK, by following standard procedures. The protein solution was centrifuged for 5 min at 13,000 × g before being measured at 4°C. Scattering curves were collected with a two-dimensional multiwire proportional counter, at sample-to-detector distances of 1 m (7 mg/ml, 100 μl) and 4.25 m (0.8, 1.6, 2.5 mg/ml, 100 μl), at a wavelength (λ) of 1.54 Å, covering the momentum transfer range of $0.008 < q < 0.78$ Å^{-1} ($q = 4\pi\sin\theta/\lambda$, where 2θ is the scattering angle). The data were collected in 30 successive 1 min frames, and they were then normalized to the intensity of the incident beam, radially integrated over a 60° sector, averaged over the frame number, and normalized to the detector response. The scattering of the buffer was then subtracted, and the low- and high-angle curves were merged over the q range of 0.05–0.15 Å^{-1}. Reproducibility of the intensity as a function of time was evidence for lack of radiation damage of the monomeric pro-MMP-9 sample, and this was further verified by SDS-PAGE (see the Supplemental Data and Figure S3). Both the forward scattering intensity, $I(0)$, and the radius of gyration (R_g) were evaluated with the program package PRIMUS (Konarev et al., 2003) by using the Guinier approximation: $I(q) = I(0)\exp(-q^2R_g^2/3)$ for $qR_g < 1.3$ (Guinier and Fournet, 1955). In addition, we used the indirect Fourier-transform program GNOM (Svergun, 1992) on the entire scattering curve. GNOM also provides the distance distribution function, $p(r)$, of the particle and its maximum dimension D_{max}, defined as the point at which $p(r)$ becomes zero. To determine $p(r)$, we assigned $p(0) = 0$ and $p(D_{max})$ free, in the first instance, to judge whether the chosen r interval was correct. D_{max} was the lowest value yielding the lowest positive $p(D_{max})$. After fixing D_{max}, $p(0)$ and $p(D_{max})$ were fixed to zero. The data were then cut at the low- and high-angle region until the $p(r)$ functions converged.

The crystal structures of the two MMP-9 domains (N-terminal catalytic domain and C-terminal hemopexin domain) were analyzed by using the program CRYSOL (Svergun et al., 1995) in order to calculate their corresponding theoretical scattering curves. These were further Fourier transformed to yield their theoretical pair distribution functions, while the D_{max} and R_g values were calculated. Ab initio modeling of the SAXS curves are described in detail in the Supplemental Data. Structural figures were made with PyMOL (DeLano, 2002).

To further confirm the accuracy of the model, its solution hydrodynamic properties were calculated by using HYDROPRO (Garcia De La Torre et al., 2000), and then compared to the experimental values. The radius of shell minibeads was varied from 2.2 to 4.2 Å in six increments. The solvent density and viscosity and the protein partial specific volume were calculated by using SEDNTERP (Laue et al., 1992). Sphere radii for the hydrodynamic shell model varied between 3.8 and 5.3 Å. The radius of the dummy residues (DRs) in the SAXS model is 3.8 Å. However, the actual dimension of the shell model is slightly larger due to protein hydration, yet the extent of enlargement is difficult to determine (Garcia De La Torre et al., 2000). It was previously suggested that increasing the DRs' radii by 1.5 Å would take into account hydration reliably (Ackerman et al., 2003).

Atomic Force Microscopy Imaging

Imaging was performed by using a multimode atomic force microscope (MMAFM Veeco/Digital Instruments, Santa Barbara, CA, USA) equipped with an E-scanner, with a maximum scan range of 14 × 14 μm^2. Samples were imaged in air or in buffer by using Tapping Mode. To obtain samples free of artifacts from spurious adsorbates, mainly salt deposition, an aggressive rinsing procedure was required. By using the amine-modified silane surfaces and the crosslinking procedure, it was possible to prepare surfaces that removed nearly all of the background (as determined by blank runs), while maintaining a significant surface concentration of the protein.

In order to minimize the amount of force applied, the amplitude set point was adjusted to the maximum value that gave a stable trace. High-resolution images of biological samples in air were obtained by using "spike" tips-DP14 "HI-RES^{TM}" probes from Mikromasch (Estonia). These probes have a resonant frequency of ~160 kHz, a force constant of ~5 N/m, and a rated radius of curvature of 2 nm or less, but they are only suitable for measurements on surfaces with an rms roughness of less then 20 nm due to the presence of additional "spikes" that could cause multiple contacts on a rough surface. DNP-S probes (Veeco) with a nominal radius of 20 nm were used for the liquid measurements, which were performed in the standard MMAFM liquid cell. The sizes of the protein molecules were determined from cross-sectional analysis. The width values were then corrected for broadening by the tip, by subtracting the tip envelope as observed from a typical high-resolution SEM image.

Supplemental Data

Supplemental Data include complete details of experimental conditions, sample preparation, and data analysis and are available at http://www.structure.org/cgi/content/full/15/10/1227/DC1/.

ACKNOWLEDGMENTS

We are grateful to Dr. Dror Noy for help with the operation of the analytical ultracentrifugation and to Ilse Van Aelst for recombinant expression studies. We also thank Drs. Samar Hasnain, Tzvia Selzer, and Claude Nogues for fruitful discussions and for critically reviewing this manuscript. This work is supported by the Minerva Foundation, the Israel Science Foundation, the Kimmelman Center at the Weizmann Institute, the Ambach family fund, the Geconcerteerde OnderzoeksActies (GOA 2007-2011), the Fund for Scientific Research-Flanders (FWO-Vlaanderen), and Excellence Financing (EF 05/015), Belgium. P.E.VdS. is a postdoctoral researcher of the FWO-Vlaanderen. I.S. is the incumbent of the Pontecorvo professorial chair.

Received: May 16, 2007
Revised: July 12, 2007
Accepted: July 31, 2007
Published: October 16, 2007

REFERENCES

Ackerman, C.J., Harnett, M.M., Harnett, W., Kelly, S.M., Svergun, D.I., and Byron, O. (2003). 19 Å solution structure of the filarial nematode immunomodulatory protein, ES-62. Biophys. J. *84*, 489–500.

Agrawal, S., Anderson, P., Durbeej, M., van Rooijen, N., Ivars, F., Opdenakker, G., and Sorokin, L.M. (2006). Dystroglycan is selectively cleaved at the parenchymal basement membrane at sites of leukocyte extravasation in experimental autoimmune encephalomyelitis. J. Exp. Med. *203*, 1007–1019.

Altschul, S.F., Madden, T.L., Schaffer, A.A., Zhang, J., Zhang, Z., Miller, W., and Lipman, D.J. (1997). Gapped BLAST and PSI-BLAST: a new generation of protein database search programs. Nucleic Acids Res. *25*, 3389–3402.

Cha, H., Kopetzki, E., Huber, R., Lanzendorfer, M., and Brandstetter, H. (2002). Structural basis of the adaptive molecular recognition by MMP9. J. Mol. Biol. *320*, 1065–1079.

Collier, I.E., Krasnov, P.A., Strongin, A.Y., Birkedal-Hansen, H., and Goldberg, G.I. (1992). Alanine scanning mutagenesis and functional analysis of the fibronectin-like collagen-binding domain from human 92-kDa type IV collagenase. J. Biol. Chem. *267*, 6776–6781.

DeLano, W.L. (2002).The PyMOL Molecular Graphics System (http://www.pymol.org).

DePristo, M.A., de Bakker, P.I., Lovell, S.C., and Blundell, T.L. (2003a). Ab initio construction of polypeptide fragments: efficient generation of accurate, representative ensembles. Proteins *51*, 41–55.

DePristo, M.A., De Bakker, P.I., Shetty, R.P., and Blundell, T.L. (2003b). Discrete restraint-based protein modeling and the Cα-trace problem. Protein Sci. *12*, 2032–2046.

Elkins, P.A., Ho, Y.S., Smith, W.W., Janson, C.A., D'Alessio, K.J., McQueney, M.S., Cummings, M.D., and Romanic, A.M. (2002). Structure of the C-terminally truncated human ProMMP9, a gelatin-binding matrix metalloproteinase. Acta Crystallogr. D Biol. Crystallogr. *58*, 1182–1192.

Emonard, H., Bellon, G., Troeberg, L., Berton, A., Robinet, A., Henriet, P., Marbaix, E., Kirkegaard, K., Patthy, L., Eeckhout, Y., et al. (2004). Low density lipoprotein receptor-related protein mediates endocytic clearance of pro-MMP-2.TIMP-2 complex through a thrombospondin-independent mechanism. J. Biol. Chem. *279*, 54944–54951.

Fridman, R., Toth, M., Chvyrkova, I., Meroueh, S.O., and Mobashery, S. (2003). Cell surface association of matrix metalloproteinase-9 (gelatinase B). Cancer Metastasis Rev. *22*, 153–166.

Garcia De La Torre, J., Huertas, M.L., and Carrasco, B. (2000). Calculation of hydrodynamic properties of globular proteins from their atomic-level structure. Biophys. J. *78*, 719–730.

Garg, P., Rojas, M., Ravi, A., Bockbrader, K., Epstein, S., Vijay-Kumar, M., Gewirtz, A.T., Merlin, D., and Sitaraman, S.V. (2006). Selective ablation of matrix metalloproteinase-2 exacerbates experimental colitis: contrasting role of gelatinases in the pathogenesis of colitis. J. Immunol. *177*, 4103–4112.

Guinier, A., and Fournet, G. (1955). Small-Angle Scattering of X-Rays (New York: John Wiley & Sons, Inc.).

Heissig, B., Hattori, K., Dias, S., Friedrich, M., Ferris, B., Hackett, N.R., Crystal, R.G., Besmer, P., Lyden, D., Moore, M.A., et al. (2002). Recruitment of stem and progenitor cells from the bone marrow niche requires MMP-9-mediated release of kit-ligand. Cell *109*, 625–637.

Hu, J., Van den Steen, P.E., Sang, Q.X., and Opdenakker, G. (2007). Matrix metalloproteinase inhibitors as therapy for inflammatory and vascular diseases. Nat. Rev. Drug Discov. *6*, 480–498.

Itoh, T., Matsuda, H., Tanioka, M., Kuwabara, K., Itohara, S., and Suzuki, R. (2002). The role of matrix metalloproteinase-2 and matrix metalloproteinase-9 in antibody-induced arthritis. J. Immunol. *169*, 2643–2647.

Konarev, P.V., Volkov, V.V., Sokolova, A.V., Koch, M.H.J., and Svergun, D.I. (2003). PRIMUS: a Windows PC-based system for small-angle scattering data analysis. J. Appl. Cryst. *36*, 1277–1282.

Kozin, M.B., and Svergun, D.I. (2001). Automated matching of high- and low-resolution structural models. J. Appl. Cryst. *34*, 33–41.

Laue, T.M., Shah, B.D., Ridgeway, T.M., and Pelletier, S.L. (1992). Analytical Ultracentrifugation in Biochemistry and Polymer Science (Cambridge, U.K.: Royal Society of Chemistry).

Lauer-Fields, J.L., Juska, D., and Fields, G.B. (2002). Matrix metalloproteinases and collagen catabolism. Biopolymers *66*, 19–32.

Li, X., Romero, P., Rani, M., Dunker, A.K., and Obradovic, Z. (1999). Predicting protein disorder for N-, C-, and internal regions. Genome Inform. Ser Workshop Genome Inform. *10*, 30–40.

Liu, Z., Shipley, J.M., Vu, T.H., Zhou, X., Diaz, L.A., Werb, Z., and Senior, R.M. (1998). Gelatinase B-deficient mice are resistant to experimental bullous pemphigoid. J. Exp. Med. *188*, 475–482.

Liu, Z., Zhou, X., Shapiro, S.D., Shipley, J.M., Twining, S.S., Diaz, L.A., Senior, R.M., and Werb, Z. (2000). The serpin α1-proteinase inhibitor is a critical substrate for gelatinase B/MMP-9 in vivo. Cell *102*, 647–655.

Maskos, K. (2005). Crystal structures of MMPs in complex with physiological and pharmacological inhibitors. Biochimie *87*, 249–263.

Masure, S., Proost, P., Van Damme, J., and Opdenakker, G. (1991). Purification and identification of 91-kDa neutrophil gelatinase. Release by the activating peptide interleukin-8. Eur. J. Biochem. *198*, 391–398.

McQuibban, G.A., Gong, J.H., Tam, E.M., McCulloch, C.A., Clark-Lewis, I., and Overall, C.M. (2000). Inflammation dampened by gelatinase A cleavage of monocyte chemoattractant protein-3. Science *289*, 1202–1206.

Monaco, S., Sparano, V., Gioia, M., Sbardella, D., Di Pierro, D., Marini, S., and Coletta, M. (2006). Enzymatic processing of collagen IV by MMP-2 (gelatinase A) affects neutrophil migration and it is modulated by extracatalytic domains. Protein Sci. *15*, 2805–2815.

Morgunova, E., Tuuttila, A., Bergmann, U., Isupov, M., Lindqvist, Y., Schneider, G., and Tryggvason, K. (1999). Structure of human pro-matrix metalloproteinase-2: activation mechanism revealed. Science *284*, 1667–1670.

Mylonas, E., and Svergun, D.I. (2007). Accuracy of molecular mass determination of proteins in solution by small-angle X-ray scattering. J. Appl. Cryst. *40*, S245–S249.

Nelissen, I., Martens, E., Van den Steen, P.E., Proost, P., Ronsse, I., and Opdenakker, G. (2003). Gelatinase B/matrix metalloproteinase-9 cleaves interferon-β and is a target for immunotherapy. Brain *126*, 1371–1381.

Olson, M.W., Bernardo, M.M., Pietila, M., Gervasi, D.C., Toth, M., Kotra, L.P., Massova, I., Mobashery, S., and Fridman, R. (2000). Characterization of the monomeric and dimeric forms of latent and active matrix metalloproteinase-9. Differential rates for activation by stromelysin 1. J. Biol. Chem. *275*, 2661–2668.

Opdenakker, G., Van den Steen, P.E., and Van Damme, J. (2001). Gelatinase B: a tuner and amplifier of immune functions. Trends Immunol. *22*, 571–579.

Opdenakker, G., Nelissen, I., and Van Damme, J. (2003). Functional roles and therapeutic targeting of gelatinase B and chemokines in multiple sclerosis. Lancet Neurol. *2*, 747–756.

Overall, C.M. (2002). Molecular determinants of metalloproteinase substrate specificity: matrix metalloproteinase substrate binding domains, modules, and exosites. Mol. Biotechnol. *22*, 51–86.

Owen, C.A., Hu, Z., Barrick, B., and Shapiro, S.D. (2003). Inducible expression of tissue inhibitor of metalloproteinases-resistant matrix metalloproteinase-9 on the cell surface of neutrophils. Am. J. Respir. Cell Mol. Biol. *29*, 283–294. Published online March 27, 2003. 10.1165/rcmb.2003-0034OC.

Petoukhov, M.V., Eady, N.A., Brown, K.A., and Svergun, D.I. (2002). Addition of missing loops and domains to protein models by x-ray solution scattering. Biophys. J. *83*, 3113–3125.

Piccard, H., Van den Steen, P.E., and Opdenakker, G. (2007). Hemopexin domains as multifunctional liganding modules in matrix metalloproteinases and other proteins. J. Leukoc. Biol. *81*, 870–892.

Receveur, V., Czjzek, M., Schulein, M., Panine, P., and Henrissat, B. (2002). Dimension, shape, and conformational flexibility of a two domain fungal cellulase in solution probed by small angle X-ray scattering. J. Biol. Chem. *277*, 40887–40892.

Roeb, E., Schleinkofer, K., Kernebeck, T., Potsch, S., Jansen, B., Behrmann, I., Matern, S., and Grotzinger, J. (2002). The matrix metalloproteinase 9 (mmp-9) hemopexin domain is a novel gelatin binding domain and acts as an antagonist. J. Biol. Chem. *277*, 50326–50332.

Rudd, P.M., Mattu, T.S., Masure, S., Bratt, T., Van den Steen, P.E., Wormald, M.R., Kuster, B., Harvey, D.J., Borregaard, N., Van Damme, J., et al. (1999). Glycosylation of natural human neutrophil gelatinase B and neutrophil gelatinase B-associated lipocalin. Biochemistry *38*, 13937–13950.

Schaffer, A.A., Aravind, L., Madden, T.L., Shavirin, S., Spouge, J.L., Wolf, Y.I., Koonin, E.V., and Altschul, S.F. (2001). Improving the accuracy of PSI-BLAST protein database searches with composition-based statistics and other refinements. Nucleic Acids Res. *29*, 2994–3005.

Siegel, L.M., and Monty, K.J. (1966). Determination of molecular weights and frictional ratios of proteins in impure systems by use of gel filtration and density gradient centrifugation. Application to crude preparations of sulfite and hydroxylamine reductases. Biochim. Biophys. Acta *112*, 346–362.

Stetler-Stevenson, W.G., Aznavoorian, S., and Liotta, L.A. (1993). Tumor cell interactions with the extracellular matrix during invasion and metastasis. Annu. Rev. Cell Biol. *9*, 541–573.

Stocker, W., and Bode, W. (1995). Structural features of a superfamily of zinc-endopeptidases: the metzincins. Curr. Opin. Struct. Biol. *5*, 383–390.

Svergun, D., Barberato, C., and Koch, M.H.J. (1995). CRYSOL - a program to evaluate x-ray solution scattering of biological macromolecules from atomic coordinates. J. Appl. Cryst. *28*, 768–773.

Svergun, D.I. (1992). Determination of the regularization parameter in indirect-transform methods using perceptual criteria. J. Appl. Cryst. *25*, 495–503.

Svergun, D.I., and Koch, M.H. (2002). Advances in structure analysis using small-angle scattering in solution. Curr. Opin. Struct. Biol. *12*, 654–660.

Svergun, D.I., Petoukhov, M.V., and Koch, M.H. (2001). Determination of domain structure of proteins from X-ray solution scattering. Biophys. J. *80*, 2946–2953.

Towns-Andrews, E., Berry, A., Bordas, J., Mant, G.R., Murray, P.K., Roberts, K., Sumner, I., Worgan, J.S., and Lewis, R. (1989). Time-resolved X-ray-diffraction station - X-ray optics, detectors, and data acquisition. Rev. Sci. Instrum. *60*, 2346–2349.

Van den Steen, P.E., Proost, P., Wuyts, A., Van Damme, J., and Opdenakker, G. (2000). Neutrophil gelatinase B potentiates interleukin-8 tenfold by aminoterminal processing, whereas it degrades CTAP-III, PF-4, and GRO-α and leaves RANTES and MCP-2 intact. Blood *96*, 2673–2681.

Van den Steen, P.E., Opdenakker, G., Wormald, M.R., Dwek, R.A., and Rudd, P.M. (2001). Matrix remodelling enzymes, the protease cascade and glycosylation. Biochim. Biophys. Acta *1528*, 61–73.

Van den Steen, P.E., Proost, P., Brand, D.D., Kang, A.H., Van Damme, J., and Opdenakker, G. (2004). Generation of glycosylated remnant epitopes from human collagen type II by gelatinase B. Biochemistry *43*, 10809–10816.

Van den Steen, P.E., Van Aelst, I., Hvidberg, V., Piccard, H., Fiten, P., Jacobsen, C., Moestrup, S.K., Fry, S., Royle, L., Wormald, M.R., et al. (2006). The hemopexin and O-glycosylated domains tune gelatinase B/MMP-9 bioavailability via inhibition and binding to cargo receptors. J. Biol. Chem. *281*, 18626–18637.

Violot, S., Aghajari, N., Czjzek, M., Feller, G., Sonan, G.K., Gouet, P., Gerday, C., Haser, R., and Receveur-Brechot, V. (2005). Structure of a full length psychrophilic cellulase from *Pseudoalteromonas haloplanktis* revealed by X-ray diffraction and small angle X-ray scattering. J. Mol. Biol. *348*, 1211–1224.

von Ossowski, I., Eaton, J.T., Czjzek, M., Perkins, S.J., Frandsen, T.P., Schulein, M., Panine, P., Henrissat, B., and Receveur-Brechot, V. (2005). Protein disorder: conformational distribution of the flexible linker in a chimeric double cellulase. Biophys. J. *88*, 2823–2832.

Werb, Z., and Chin, J.R. (1998). Extracellular matrix remodeling during morphogenesis. Ann. N Y Acad. Sci. *857*, 110–118.

Wilhelm, S.M., Collier, I.E., Marmer, B.L., Eisen, A.Z., Grant, G.A., and Goldberg, G.I. (1989). SV40-transformed human lung fibroblasts secrete a 92-kDa type IV collagenase which is identical to that secreted by normal human macrophages. J. Biol. Chem. *264*, 17213–17221.

Williamson, M.P. (1994). The structure and function of proline-rich regions in proteins. Biochem. J. *297*, 249–260.

Wolf, K., Mazo, I., Leung, H., Engelke, K., von Andrian, U.H., Deryugina, E.I., Strongin, A.Y., Brocker, E.B., and Friedl, P. (2003). Compensation mechanism in tumor cell migration: mesenchymal-amoeboid transition after blocking of pericellular proteolysis. J. Cell Biol. *160*, 267–277.

Yang, Z., Strickland, D.K., and Bornstein, P. (2001). Extracellular matrix metalloproteinase 2 levels are regulated by the low density lipoprotein-related scavenger receptor and thrombospondin 2. J. Biol. Chem. *276*, 8403–8408.

Yu, Q., and Stamenkovic, I. (2000). Cell surface-localized matrix metalloproteinase-9 proteolytically activates TGF-β and promotes tumor invasion and angiogenesis. Genes Dev. *14*, 163–176.

